

Synchrotron X-Ray Study of Bulk Lattice Strains in Externally Loaded Cu-Mo Composites

ALEXANDER WANNER and DAVID C. DUNAND

A synchrotron X-ray transmission technique was applied to study the internal load transfer and micromechanical damage in molybdenum particle-reinforced copper matrix composites during plastic deformation. Mechanically loaded, 1.5-mm-thick specimens were irradiated with a monochromatic beam of 65 keV X-rays. Low-index diffraction rings of both phases were recorded with a high-resolution two-dimensional detector. By means of newly developed data processing routines, we could quantify as a function of applied stress both the ring distortion (from which the volume-averaged elastic strains in the two phases were calculated), and the ring graininess (which is related to the Bragg peak broadening). Based on this information, the deformation and damage processes in these alloys were studied in detail. As compared to conventional neutron diffraction methods, the photon transmission technique yielded similar precision but at much reduced measurement times. The main sources of experimental errors were identified and strategies to minimize these errors were developed.

I. INTRODUCTION

THE load-bearing capacity of a metal matrix composite (MMC) is dictated by the load transfer occurring from the compliant, soft matrix to the stiff, hard reinforcements.^[1] The load partitioning ratio between matrix and reinforcement remains constant as long as both components behave in a linear elastic manner. Upon plastic deformation of the matrix, the partitioning ratio changes and the reinforcing phases carry a greater portion of the load. Thus, the composite becomes mechanically more efficient as a higher portion of the applied load is carried by the reinforcing phase. However, with increasing stress in the reinforcement, that phase may fracture or debond from the matrix, thus reducing the load born by the reinforcement and the overall load-bearing capacity of the composite, and also often leading to macroscopic failure of the composite.

Experimental measurement of load partitioning between the individual phases of MMCs can thus give a wealth of information on the micromechanical evolution of composites during deformation. Such measurements have been performed by neutron diffraction in aluminum reinforced with various ceramic particles,^[2,3,4] in NiTi reinforced with TiC particles,^[5,6] and in a model composite consisting of copper reinforced with molybdenum particulates.^[7] Neutron diffraction techniques, however, require long measurement times and large diffraction volumes because of the small neutron flux available at existing thermal neutron sources and the inherently weak interaction of neutrons with crystalline solids.^[8] The availability of high-energy, high-intensity X-rays from third-generation synchrotron research facilities has allowed the use of X-rays for such bulk strain measurements. Recently, Daymond and Withers,^[9] and Korsunsky *et al.*^[10] have described a novel synchrotron X-ray transmission technique by which, as they demonstrated in their studies on

fine-grained aluminum matrix composites, bulk strain measurements can be performed at much reduced exposure times and in small diffracting volumes, thus allowing for investigating the time dependence of lattice strains and for mapping such strains with a lateral resolution of a fraction of a millimeter.

We have further developed this technique and applied it to study lattice strains in copper-molybdenum composites.^[11] The first goal of the present work is to establish a detailed methodology for lattice strain measurements in mechanically loaded samples. As there is only limited experience with this technique and as the methods to evaluate the raw data are not standardized, the present article examines in detail the experimental procedures and data evaluation techniques. The major sources of experimental error are identified and appropriate measures to minimize these errors are discussed. The second goal of the present study is to compare, on Cu-Mo composites from the same origin, the phase strain measured by neutron diffraction (as reported by Daymond *et al.*^[7,12]) and by synchrotron X-ray diffraction (as reported in the present paper), thus establishing a direct comparison between the two techniques. Finally, the third goal of this article is to use these Cu-Mo composites to further investigate how phase strain partitioning during mechanical loading is affected by varying reinforcement volume fraction and by matrix plastic deformation reinforcement damage occurring at large macroscopic plastic strains.

II. EXPERIMENTAL PROCEDURES

A. Materials

We used copper matrix composites with nominal contents of 7.5 or 15 vol pct molybdenum particulates (referred to in the following as Cu-7.5Mo and Cu-15Mo) fabricated by powder metallurgy for the neutron diffraction study by Daymond *et al.*,^[7,12,13] thus allowing a direct comparison with that study. Daymond *et al.*, however, only investigated the Cu-15Mo composite. The starting materials were 99.9 pct pure, spherical copper powder (from Aremco Products, Ossining, NY), less than 44 μm in size, and 99.8 pct pure

ALEXANDER WANNER, Akademischer Rat, is with the Institute für Metallkunde, Universität Stuttgart, D-70174 Stuttgart, Germany. DAVID C. DUNAND, Associate Professor, is with the Department of Materials Science and Engineering, Northwestern University, Evanston, IL 60208. Manuscript submitted February 8, 2000.

molybdenum powder (from Atlantic Equipment Engineers, Bergenfield, NJ), with a reported size range of 10 to 44 μm . The molybdenum powder particulates exhibit a complex morphology as they are partially sintered aggregates of fine, micron-size molybdenum particles.

The powder blends were packed in steel cans, which were lined with molybdenum foil to prevent contamination by diffusion from the steel. The powders were first annealed in the can at 850 °C under hydrogen to reduce any oxides. The evacuated and sealed cans were subsequently densified by hot isostatic pressing (HIP) at 900 °C and 100 MPa for 125 minutes. Below the eutectic temperature of 1083.4 °C, Cu and Mo exhibit very little mutual solubility.^[14] Therefore, these Cu/Mo composites produced by solid-state powder metallurgy are expected to be composed of the two pure, untextured phases. Also, unreinforced copper billets were produced from the copper powder using the same HIP route for comparison purposes.

B. Measurements

1. Material composition and microstructure

The as-fabricated composites and the reference material were examined with respect to chemical composition and microstructure. The volume fractions of reinforcement (point counting method) and the matrix grain size (linear intersect method) were measured on optical micrographs of as-polished and of etched metallographic sections, respectively. In addition, the morphologies of the reinforcement particulates were studied by scanning electron microscope (SEM) on loose powder used to fabricate the composites and on polished cross sections of the consolidated composites.

2. Mechanical tests

Dogbone-shaped, flat tensile specimens with gages 8-mm long, 3-mm wide, and 1.5-mm thick were fabricated from bulk densified composites by electric discharge machining and subsequent mechanical polishing. Uniaxial tensile tests were performed at room temperature using the miniature, screw-driven tensile device described by Noyan and Cohen.^[8] First, *ex-situ* tests on dedicated specimens were performed to obtain the tensile stress-strain curves of the materials. During these tests, the specimen strain was measured continuously using glue-on resistor strain gages. *In-situ* tensile tests without strain gages were carried out at a bending magnet beamline of the Advanced Photon Source at Argonne National Laboratories (Argonne, IL.). The tensile stress was increased stepwise (usually in steps of 25 MPa) and held constant during exposure times.

3. Lattice strain measurements by x-ray diffraction experiments

The general experimental setup for the type of high-energy X-ray transmission experiments performed in the present study was first described in a recent article by Daymond and Withers.^[9] The polycrystalline specimen is irradiated with a monochromatic, parallel beam of high-energy X-rays, and complete, ring-shaped diffraction patterns are recorded with a two-dimensional detector, as shown schematically in Figure 1. Unlike Daymond and Withers, we attached a calibration powder to the specimen, as described in more detail later. The specimen was irradiated by a parallel beam of 65 keV photons (corresponding to a wavelength of $\lambda \approx 0.19 \text{ \AA}$) with approximate dimensions $0.2 \times 0.2 \text{ mm}$ and

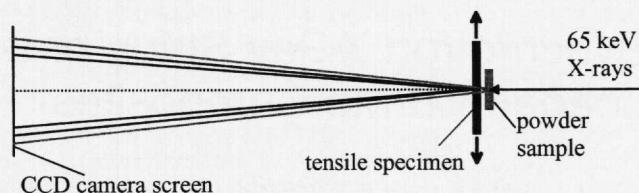


Fig. 1—Sketch of experimental arrangement for the high-energy photon diffraction experiments performed in the present study.

positioned approximately in the center of the gage section and parallel to the sample thickness. Hence, the path length of the incident beam inside the specimen was 1.5 mm and the diffracting volume, over which the average strain results were measured, was about 0.06 mm^3 .

The diffraction geometry is similar to that in a transmission electron microscope in the sense that the wavelength of the high-energy X-rays is considerably smaller than the typical spacings of low-index lattice planes of highly symmetric crystals. As a consequence, the Bragg angles corresponding to low-index planes are small, which means that these planes are oriented almost parallel to the incident beam when they are in diffracting condition. This allows for recording the strains present in the plane perpendicular to the incident beam, and this plane contains the longitudinal direction (loading axis) as well as a transverse direction of the specimen under investigation.

The ringlike diffraction patterns produced on a plane normal to the incident beam were recorded using a charge-coupled device (CCD) camera fabricated by MAR, Inc. (Evanston, IL) providing 16-bit intensity readings over a circular screen 132 mm in diameter consisting of an orthogonal array of square, $64 \times 64 \mu\text{m}$, pixels. The total exposure time was always 600 seconds. The readings obtained during the first half of that exposure time were correlated with those obtained during the second half in order to eliminate spotlike, stochastic spurious readings presumably caused by background radiation. This was accomplished using an image processing routine included with the software package MARCCD v. 3.19 (MAR, Inc.) that was also used for control and data acquisition of the CCD camera. The distance L between the CCD screen and the specimen was set to 510 mm, which allowed for simultaneous recordings of all rings with diffraction angles $\theta \leq 3.7 \text{ deg}$. A typical diffraction pattern recorded by the CCD camera is shown in Figure 2, showing the Mo (110) ($\theta = 2.46 \text{ deg}$), Cu (111) ($\theta = 2.62 \text{ deg}$), Cu (200) ($\theta = 3.02 \text{ deg}$), and Mo (200) ($\theta = 3.48 \text{ deg}$) rings from the specimen as well as the Fe (110) ($\theta = 2.70 \text{ deg}$) ring from an iron powder sample inserted into the X-ray beam for error correction purposes. This iron powder was filled in a small container, which was fixed directly to the specimen gage section using rubber bands. The container consisted of two flat, parallel polyethylene windows, 1.04 mm in thickness, separated by a 1.46-mm-thick spacer. The distance ΔL between the centers of the calibration powder and of the specimen was 2.52 mm. The X-ray beam was thus transmitted through the 1.5-mm-thick composite sample, the 1.5-mm-thick, loosely compacted iron powder, and the two 1-mm-thick, amorphous polymer plates used for the container. Iron was chosen because its diffraction rings do not overlap with those of Mo or Cu and because it has high diffraction efficiency as compared to silicon, the only other

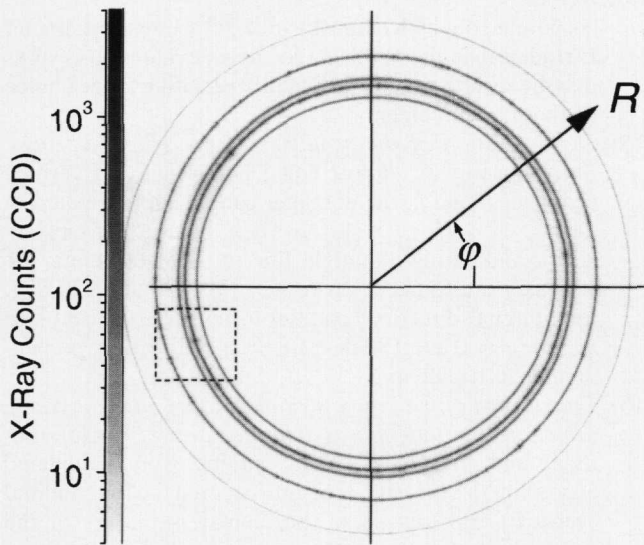


Fig. 2—Typical diffraction pattern as recorded by the two-dimensional detector (CCD camera) showing concentric diffraction rings of Cu and Mo from as-fabricated Cu-15Mo composite under zero applied stress and of Fe from powder sample affixed to the gage section of the specimen. The ring sequence from inside to outside is Mo (110), Cu (111), Fe (110), Cu (200), and Mo (200). An enlargement of the delineated area is found in Fig. 12.

standard we investigated for calibration. Depending on the sample under investigation, however, it may be necessary to use a different calibration substance.

III. ANALYSIS OF DIFFRACTION PATTERNS

A. Lattice Strains

The diameters of a diffraction ring D on the camera screen, the diffraction angle θ , and the specimen-to-camera distance L are connected by simple trigonometry as

$$\theta = \frac{1}{2} \arctan \left(\frac{D}{2L} \right) \quad [1]$$

The lattice spacing d of the diffracting set of planes is obtained from Bragg's equation as

$$d = \frac{\lambda}{2 \sin \theta} \quad [2]$$

where λ is the wavelength of the X-rays. Combining the preceding two equations gives

$$d = \frac{\lambda}{2 \sin \left(\frac{1}{2} \arctan \left(\frac{D}{2L} \right) \right)} \quad [3]$$

For small Bragg angles ($D/2L \ll 1$), the trigonometric functions in Eq. [3] can be replaced by their arguments, which yields the much simpler equation

$$d \approx \frac{2\lambda L}{D} \quad [4]$$

For the lattice strain ε calculated with respect to a reference state denoted by superscripts 0, we can write

$$\varepsilon = \frac{d - d^0}{d^0} \approx \frac{D^0 - D}{D} \approx \frac{D^0 - D}{D^0} \quad [5]$$

This simple equation, which has widely been used to evaluate the kind of diffraction patterns produced by the present technique,^{9,10} is based on the tacit assumption that the product λL in Eq. [1] is unchanged for the two independent diameter measurements D and D_0 . In many practical cases, however, this assumption may not be fully justified. The specimen-to-camera distance L may change due to small positioning errors as the specimen is translated nominally perpendicularly to the beam axis for mapping purposes or as the specimen is manipulated in any other way, e.g., by applying external forces during *in-situ* mechanical tests such as those performed in the present study. With the nominal specimen-to-camera distance used in our study, an unintentional specimen displacement of only 0.1 mm in the direction of the beam would cause a spurious lattice strain of about 200 μ strains. Also, the stability of the wavelength λ with respect to mean value and bandwidth is dependent on the performance of the synchrotron as a whole and of the monochromator used in the experiment. If λ and/or L change during a series of measurements, misleading results may result, and it is difficult or even impossible to identify the artifacts in retrospect and apply appropriate corrections. We thus rewrite Eq. [5] in a more general manner as

$$\varepsilon \approx 1 - \frac{D}{D^0} \cdot \frac{\lambda^0 L^0}{\lambda L} \quad [6]$$

As shown below, the spurious strains stemming from λL changes in Eq. [6] can be eliminated by taking into account an additional diffraction ring produced by an unstrained calibration substance (powder sample) positioned in the path of the X-ray beam. In the following, the quantities related to the calibration substance and the specimen are denoted by subscripts C and S , respectively. As the lattice spacing d_C of the unstrained calibration substance does not change during the series of *in-situ* measurements, we obtain using Eq. [6]

$$\varepsilon_C = 0 \approx 1 - \frac{D_C}{D_C^0} \cdot \frac{\lambda^0 L_C^0}{\lambda L_C} \quad [7]$$

from which it follows that

$$\frac{\lambda L_C}{\lambda^0 L_C^0} \approx \frac{D_C}{D_C^0} \quad [8]$$

If the spacing $\Delta L = L_S - L_C$ remains unchanged during the measurements and is also much smaller than the specimen-to-camera distance L_S (in our case $\Delta L/L_S = 2.52/510 = 0.005$), we can write

$$\frac{L_S}{L_S^0} \approx \frac{L_C}{L_C^0} \quad [9]$$

By combining Eqs. [6], [8], and [9], we then obtain an expression for ε_S that is robust against small changes of λ and against cooperative movement of specimen and calibration substance along the beam axis during the experiment

$$\varepsilon_S = \frac{d_S - d_S^0}{d_S^0} \approx 1 - \frac{D_S}{D_S^0} \cdot \frac{D_C^0}{D_C} \quad [10]$$

As the composites of the present study were produced by

HIP, we can assume that they are texture free and quasi-isotropic. Residual stresses on a microstructural scale probably exist due to the thermal expansion mismatch between copper and molybdenum. However, the volume averages of the phase stresses must be of entirely hydrostatic nature, *i.e.*, the volume-averaged lattice strains are independent of the direction of measurement. In the present study, we do not attempt to measure these initial lattice strains but restrict our analysis to the additional strains that develop in the course of deformation under an applied uniaxial tensile stress. Because of the simple uniaxial testing conditions, two measurements in the directions parallel and perpendicular to the tensile loading axis are sufficient to characterize the strain state of the specimens.

Under ideal conditions, the diffraction patterns are initially composed of perfect, concentric circles, which are distorted during the tensile deformation of the specimen into a shape assumed to be an ellipse. As the semiaxes of these ellipses are oriented parallel and perpendicular to the direction of loading, the simplest approach to evaluate these data would be to merely measure the diameters of the diffraction rings in the horizontal and vertical directions. Daymond and Withers^[9] have demonstrated that this approach is successful under optimal experimental conditions (extremely smooth diffraction rings due to very small grain size and a favorable texture in the specimen material enhancing the diffracted intensity for their specific diffracting conditions). In the course of the present study, however, it became apparent that the diffraction rings exhibited a noticeable graininess, giving rise to very poor strain resolution if narrow horizontal and vertical strips extracted from the CCD camera image were used to determine the semiaxes.

We therefore developed an algorithm, which in some aspects is similar to that recently published by Korsunsky *et al.*^[10] and which takes the whole diffraction rings into account, thus reducing the effect of graininess on the strain results. This algorithm was implemented using the programming language IDL[®] 5.1 (Research Systems, Boulder, CO) and consists of the following steps.

- (1) *Identification of the center of the pattern.* This was accomplished by analyzing the Fe (200) peaks in horizontal and vertical cross sections cutting the diffraction pattern approximately in the middle. These intensity profiles were created by averaging over relative narrow (48 pixels wide) strips.
- (2) *Polar rebinning of pixel intensity data into radius/angle (R/φ) with respect to the pattern center.* This procedure was performed by considering 1600 radial lines in φ steps of 0.225 deg. For each φ step, the intensity was read out in intervals of $\sim 1/10$ camera pixel. In order to save computation time and data storage space, rebinning was performed only over relatively narrow radial ranges (40 pixels in width) encompassing the diffraction ring under consideration.
- (3) *Gaussian peak fitting in R at each of the 1600 angular positions.* The graininess of the rings causes the fitting routine to fail or produce implausible results in a small fraction (< 1 pct) of angular positions. These data points were eliminated using appropriate filtering routines and disregarded in the following strain analysis.
- (4) *Addition of the Gaussian center positions of diametrically opposite peaks to obtain the ring diameter $D(\varphi)$.*

As pointed out by Korsunsky *et al.*,^[10] using the diameter D (rather than the radius R) for strain evaluation ensures that the results are not particularly sensitive to the choice of the pattern center.

- (5) *Determination of the semiaxes of the elliptical rings.* For ellipses with almost equal horizontal and vertical semiaxes a and b , the diameter can be approximated as $D(\varphi) = a + (b - a) \sin^2 \varphi$. Then, by plotting $D(\varphi)$ vs $\sin^2 \varphi$ and fitting a straight line to the data points, the semiaxes are found at $\sin^2 \varphi = 1$ ($\varphi = 90$ and 270 deg; longitudinal direction, parallel to tensile axis) and $\sin^2 \varphi = 0$ ($\varphi = 0$ and 180 deg; transverse direction, perpendicular to tensile axis).
- (6) *Calculation of the lattice strains in axial and transverse directions for both phases of the composite.* The longitudinal and transverse elastic strains were calculated according to Eq. [10] taking into account the longitudinal (vertical) and transverse (horizontal) semiaxes of the diffraction rings from the specimen and the calibration substance.

As mentioned previously, this algorithm is in some aspects similar to that recently described by Korsunsky *et al.*^[10] However, our algorithm differs in an important aspect, *i.e.*, the averaging sequence. While Korsunsky *et al.* first averaged the X-ray intensities over ring segments spanning a 15 deg angle and then performed Gaussian peak fitting to obtain an average diameter for that segment, we first performed the Gaussian fitting at a high number of φ positions and then fitted an ellipse to the resulting diameter data. We also note that our ellipse fitting procedure was simplified by the fact that the directions of the semiaxes were defined by the direction of the applied stress; however, the $\sin^2 \varphi$ method proposed here can easily be adapted to more general cases by introducing an offset angle as an additional fit parameter. While more computation intensive, our procedure has two advantages. First, every angular direction has the same statistical weight, independent of the signal intensity. This is very helpful for the evaluation of grainy diffraction rings, because the information from the weak-intensity gaps between high-intensity speckles forming the ring is fully taken into account. Second, the availability of Gaussian peak fit data obtained at a large number of different φ positions can be used to characterize the graininess itself, which, as described in the following section, offers additional insight into the deformation processes occurring within the material.

B. Assessment of the Graininess of the Diffraction Rings

While a grainy diffraction ring is generally not desirable from the point of view of strain measurement, the present study shows that the graininess can offer valuable information on the microstructural and micromechanical evolution in the specimen during deformation. It was established during the course of the analysis that the 1600 Gaussian peak (half-)width values determined in different directions (1600 φ steps of 0.225 deg, as described previously) are an excellent data base to assess the graininess, as they allow for the calculation of statistical quantities such as the average and standard deviation of the ring width, A_w and S_w . These two quantities were determined for all Cu (111) and Mo (110) diffraction rings used for the strain analysis.

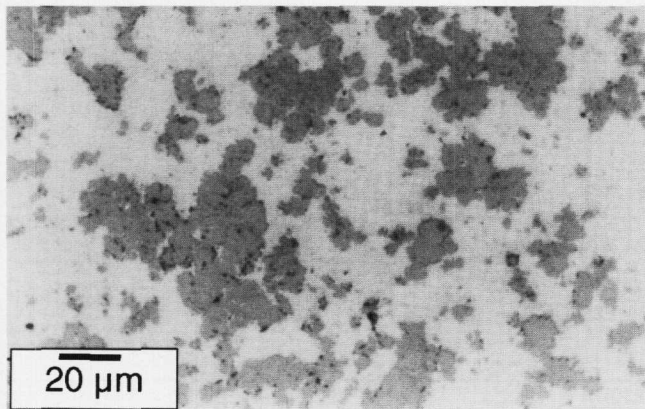


Fig. 3—Optical micrograph showing the typical microstructure of the as-fabricated Cu-15Mo composite. The apparent volume fraction of reinforcement (dark) is considerably higher than the volume fraction of Mo phase, because the reinforcements exhibit a two-phase Mo/Cu microstructure, which is not resolved by the optical microscope.

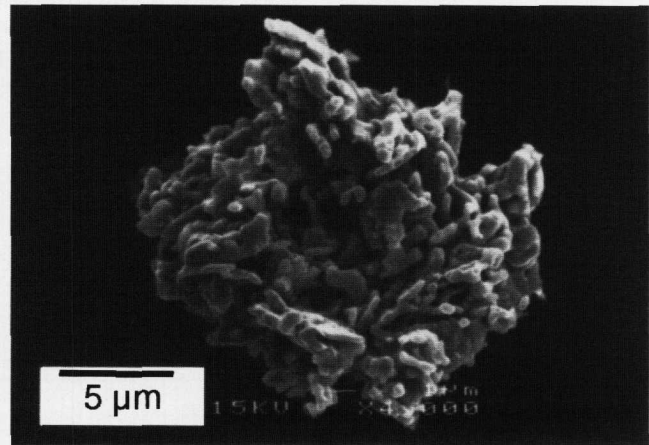


Fig. 5—SEM micrograph of a typical particulate of the Mo powder used to fabricate the Cu/Mo composites.

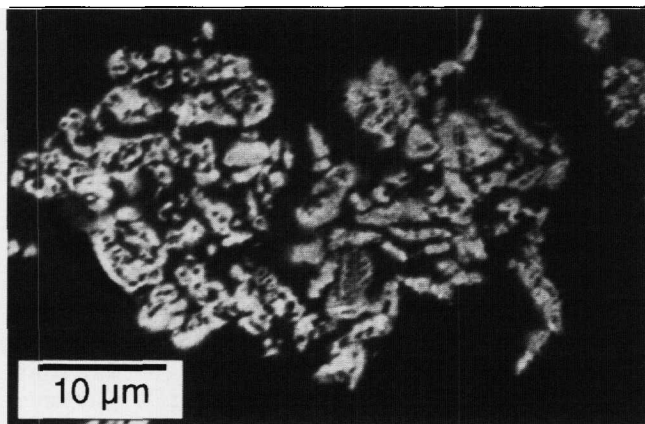


Fig. 4—SEM backscatter micrograph showing the two-phase microstructure of the reinforcements (dark phase is copper, and light phase is molybdenum).

IV. RESULTS

A. Microstructure and Stress-Strain Curves

Figure 3 is a representative optical micrograph of the Cu-15Mo composite, showing that consolidation was effective. The irregularly shaped reinforcement particulates are approximately equiaxed and reasonably well distributed in the matrix. The same observations were made on the Cu-7.5Mo composite. A closer examination of the reinforcements using an SEM operated in backscatter mode (Figure 4) shows that the particulates exhibit a two-phase, interpenetrating microstructure without any significant porosity. A likely explanation is that the initially porous molybdenum powder particulates, a typical example of which is shown in Figure 5, were completely filled with copper forced into the fine porosity during solid-state consolidation. Due to the limited resolution of the optical microscope, however, the reinforcements appear to be single phase in Figure 3. Quantitative metallographic examination of optical micrographs yielded for both composites a volume fraction of reinforcement particulates roughly twice the nominal volume fraction of molybdenum phase (Table I), indicating that the volume

fraction of molybdenum within the particulates is about 50 pct. The grain sizes in the copper matrix are listed in Table I, along with other microstructural data and the results of chemical analysis.

Figure 6 shows the engineering stress-strain curves of the two composites measured in the *ex-situ* (solid lines) and *in-situ* (data points connected by dashed lines) uniaxial tensile tests. For comparison, the curve of the unreinforced reference material (produced by HIP of Cu powder) is also presented. As expected, the Cu-15Mo composite exhibits the highest yield strength and strain hardening, and the stress-strain curve of the Cu-7.5Mo composite is bracketed by the curves of the Cu-15Mo composite and the unreinforced copper.

B. Lattice Strains

To illustrate the most crucial steps of the X-ray data evaluation procedure, exemplary D vs $\sin^2 \varphi$ plots from step (5) of the algorithm described previously are presented in Figure 7. In this set of diagrams, data from one ring of each phase of the virgin Cu-15Mo specimen mounted to the tensile rig and from the Fe powder attached to that specimen (Fig. 7a-c) are compared with corresponding data obtained when a tensile stress of 236 MPa was applied to the specimen (Fig. 7d-f). The Fe (110) data show little scatter due to the smoothness of this diffraction ring, while the data from both phases of the composite, especially those from the copper matrix in the unloaded state, exhibit a considerable amount of scatter. This underlines the importance of applying an appropriate fitting procedure. Ideally, in the unstrained state, all diffraction rings should be perfectly circular, *i.e.*, their diameters should not depend on φ and the slopes of straight lines fitted to the data presented in Figures 7(a) through (d) should be zero. However, these diagrams show that even in the unloaded state, the recorded diffraction rings are slightly elliptical, with the deviation between the semiaxes being a fraction of a pixel. Two effects may be responsible for this phenomenon: (1) the camera screen was not oriented perpendicular to the X-ray beam, and (2) the camera pixels are not arranged in a perfectly square array. These imperfections of the experimental setup are, however, not harmful, as they do not affect the final lattice strain results.

Table I. Results of Chemical and Microstructural Characterization

| Material | Cu | Cu-7.5Mo | Cu-15Mo |
|--|--------------------------------|--|--|
| Nominal chemical composition* | Mo: 0 wt pct Cu: 100 wt pct | Mo: 9.3 wt pct (7.5 vol pct) Cu: 90.7 wt pct (92.5 vol pct) | Mo: 16.8 wt pct (15 vol pct) Cu: 83.2 wt pct (85 vol pct) |
| Chemical analysis** | | Mo: (5.94 ± 0.05) wt pct Cu: (93.7 ± 0.5) wt pct | Mo: (16.73 ± 0.08) wt pct Cu: (83.07 ± 0.4) wt pct |
| Volume fraction of two-phase particulates† | 0 vol pct | (16.0 ± 2.3) vol pct | (30.0 ± 2.3) vol pct |
| Grain size of Cu matrix‡ | 25 μm | 8.8 μm | 6.4 μm |

*From powder weighing before densification.

**From X-ray fluorescence analysis of densified composites.

†From point counting analysis on optical micrographs of composites.

‡From linear intersect method on optical micrographs in the matrix region surrounding the two-phase particulates.

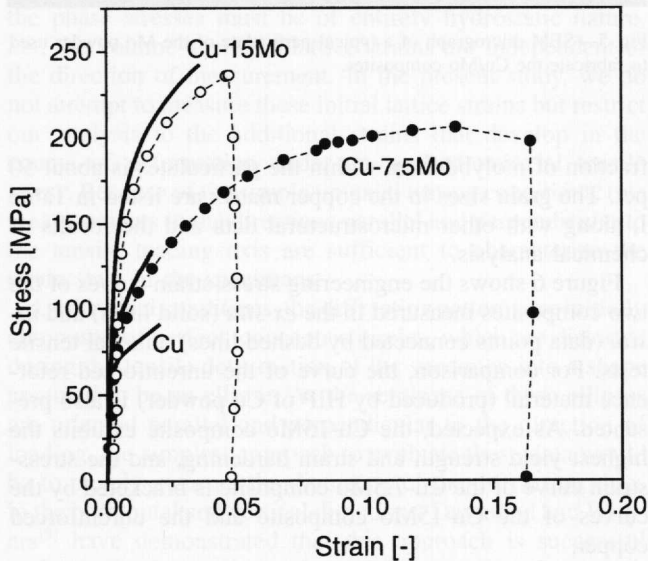


Fig. 6—Engineering stress-strain curves from *ex-situ* (solid lines) and *in-situ* (data points connected by dashed lines) uniaxial tensile tests. In the *ex-situ* tests, the strain was measured using glue-on resistor strain gages. For the *in-situ* tests, the strain was calculated from the crosshead displacement, taking into account the compliance of the miniature tensile device.

The semiaxes of the Fe (110) ellipse are different in Figures 7(a) and (d) indicating that λ and/or L must have changed between the two exposures. In Figure 8, the stress applied to the tensile specimen is plotted against the relative changes of the Fe (110) semiaxes, $(D^0_C - D_C)/D^0_C$. According to Eq. [5], these relative changes are equal to the spurious strains that would be added unnoticed to the true lattice strains of the two phases of the specimen if the measurements were performed without the calibration substance. The necessary corrections, which are accomplished by using Eq. [10] to evaluate the true lattice strains, are in fact quite large, up to almost 1000 μ strains. Based on the observation that semiaxes of the ring from the unstrained calibration substance change systematically as a function of the applied stress, it can be concluded that these changes are mainly due to specimen displacement along the direction of the X-ray beam. Considering the nominal specimen-to-camera distance of 510 mm, the range of specimen displacement must have been about 0.5 mm. Figure 8 also shows that most of the specimen displacements occurred at stresses below about 50 MPa, *i.e.*, when the load is first applied at the beginning of the tensile test and when it is completely

removed at the end of the test. Very similar stress-displacement relationships were found for all other tensile tests performed in the present study.

In Figure 9, corrected lattice strain results from two tensile tests performed on two different Cu-15Mo specimens are shown. In this diagram, the applied uniaxial stress is plotted against the volume-averaged lattice strain measured in the Mo phase in the longitudinal direction. The lattice strain results were calculated based on Eq. [10], using the vertical semiaxes of the Mo (110) and Fe (110) diffraction rings. These results have excellent reproducibility, with the largest deviations between the two curves being less than 100 μ strains.

In Figures 10(a) through (d) the complete set of lattice strain results from one of the two tensile tests performed on a Cu-15Mo specimen is shown. These diagrams include longitudinal and transverse lattice strains from evaluating the Cu (111), Cu (200), Mo (110), and Mo (200) diffraction rings, all corrected using the Fe (110) ring. It is apparent that the strain varies between phases, as expected from their different mechanical properties, and also between crystallographic directions for each phase, due to the elastoplastic anisotropy of the individual grains. In Figures 10(a) through (d) all curves show three regions with different slopes during mechanical loading, indicative of changes in the load sharing between matrix and reinforcement. In all cases, the curves obtained upon mechanical unloading of the composite are linear within measurement error (for clarity, the transverse strain unloading curves are not shown). After unloading, the longitudinal residual lattice strains are positive for the reinforcement and negative for the matrix.

Figures 11(a) through (d) show for the Cu-7.5Mo composite the same information as Figures 10(a) through (d) for the Cu-15Mo composite, which was strained to a higher stress but lower plastic strain. The lattice strain results are qualitatively similar between the two composites. The change of slope observed in the high-stress regime is far more pronounced in Cu-7.5Mo, leading to a full reversal of the lattice strain evolution in the Mo phase; *i.e.*, the lattice strain decreases with increasing applied stress. The Mo (200) diffraction ring from this material was too grainy to yield consistent results, so no data are presented. For the same reason, no data are presented from the unreinforced copper for which diffraction patterns consisted only of very few, very intense spots not amenable to the strain evaluation procedures described previously.

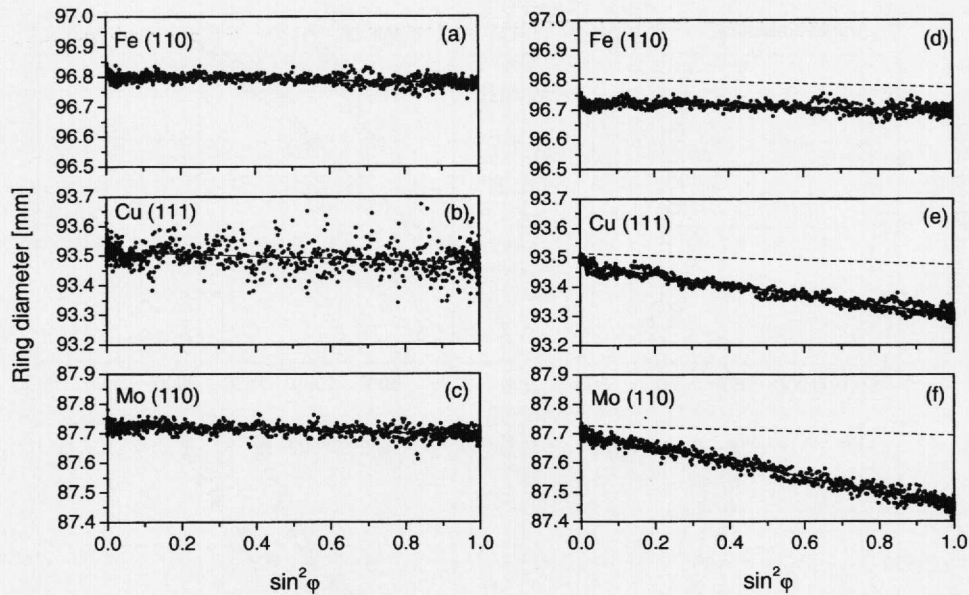


Fig. 7—Plots of $D(\varphi)$ vs $\sin^2 \varphi$ of the Fe (110), Cu (111), and Mo (110) diffraction rings. (a) through (c) unloaded, as fabricated Cu-15Mo specimen; (d) through (f) same specimen loaded *in-situ* to 236 MPa tensile stress. The dashed lines in the latter diagrams are best linear fits to the corresponding data from the unloaded specimen.

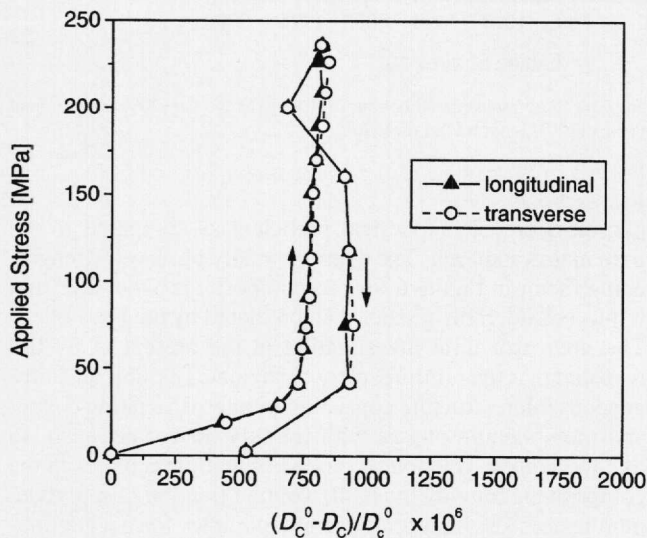


Fig. 8—Variation of the size of Fe(140) diffraction ring due to cooperative movement of the specimen and the attached calibration substance (Fe powder) during the *in-situ* tensile test. The relative changes of the semiaxes are equal to the apparent specimen lattice strains that would exist if no correction procedure was applied.

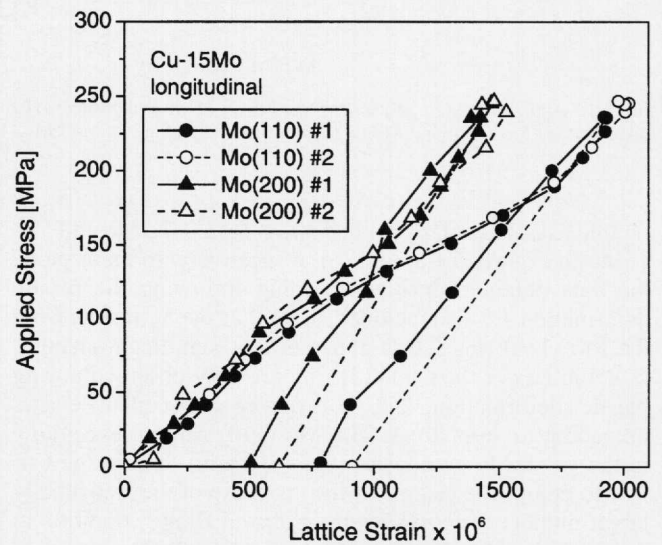


Fig. 9—Applied stress vs longitudinal lattice strain in the Mo phase of the Cu-15Mo composite. Results of two independent measurements are shown, indicating good reproducibility.

C. Evolution of the Diffraction Ring Graininess

Diffraction ring graininess, which can be expressed as the angular variation of ring intensity, was found to evolve for the copper phase in the course of the *in-situ* experiments, while it was essentially constant for the molybdenum phase. This is illustrated in Figures 12(a) and (b), which show closeups of diffraction patterns recorded for the Cu-15Mo composite in the initial unloaded state and for a stress $\sigma = 236$ MPa, respectively. In these figures, the initially grainy Cu (111) ring appears considerably smoother after the specimen has been plastically deformed. For all Cu and Mo rings

evaluated, the average ring width A_W always lay in the range of 130 to 150 μm initially and did not change by more than 10 pct as the specimen was deformed. However, the ring width standard deviation S_W was more sensitive to the changes in ring graininess. In Figure 13, S_W for the Cu (111) ring is shown as a function of the applied composite strain. The initial S_W values depend on the matrix content ($S_W \approx 45 \mu\text{m}$ for Cu-7.5Mo, and $S_W \approx 25 \mu\text{m}$ for Cu-15Mo). For both composites, a monotonic decrease of S_W with increasing strain was observed, and both curves asymptotically reached about the same level ($S_W \approx 8 \mu\text{m}$, corresponding to only about 7 pct of the average width A_W). The value of S_W is

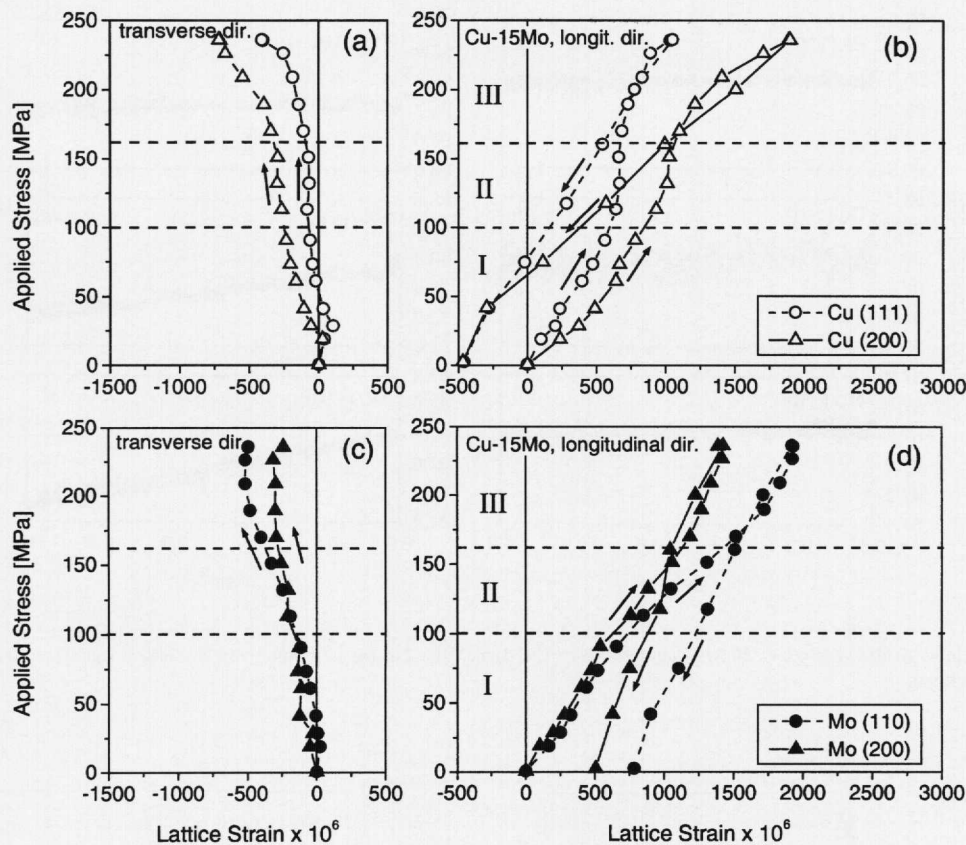


Fig. 10—Applied stress vs lattice strain for the Cu-15Mo composite. (a) Cu (111) and Cu (200), transverse direction; (b) Cu (111) and Cu (200), longitudinal direction; (c) Mo (110) and Mo (200), transverse direction; and (d) Mo (110) and Mo (200), longitudinal direction.

plotted as a function of applied stress for Cu-7.5Mo and Cu-15Mo in Figures 14(a) and (b), respectively. In these plots, the data obtained during unloading following the plastic deformation are also included, as well as the S_W results from the Mo (110) rings. It is apparent that significant changes in graininess of the Cu (111) ring are only observed during plastic deformation, but not during subsequent elastic unloading to zero stress. The Mo (110) ring is less grainy in the Cu-15Mo composite ($S_W \approx 10 \mu\text{m}$) than in the Cu-7.5Mo composite ($S_W \approx 18 \mu\text{m}$) because of the statistically larger number of molybdenum grains in Bragg condition in the former material. As mentioned earlier, the graininess of the Mo (110) rings for both composites did not change significantly throughout the whole tensile tests.

V. DISCUSSION

A. Macroscopic Stress-Strain Curves

Daymond *et al.*,^[7] who first studied the Cu-15Mo composite, have pointed out that the strengthening effect visible in the composite stress-strain curves of Figure 6 is considerably higher than expected from continuum-mechanics finite-element (FE) models. In these models, the reinforcement was represented by 15 vol pct of either spherical or cylindrical molybdenum particles embedded in a copper matrix exhibiting the same flow characteristics as the unreinforced copper material produced by powder metallurgy. For an applied strain of 0.01, these models predict a flow stress for the Cu-15Mo composite higher by a factor 1.43 (cylindrical

particles) or 1.25 (spherical particles) as compared to the pure matrix material. The experimentally observed strengthening factor in Figure 6 for this composite is about 2.25 and it is thus considerably greater than predicted by the FE models. The microstructural investigation in the present study has revealed that the reinforcement particulates exhibit a heterogeneous microstructure consisting of interpenetrating copper and molybdenum phases with roughly 50 vol pct each, so that the volume fraction of reinforcement particulates in the composite is roughly twice the volume fraction of molybdenum phase. The hard molybdenum particles form a continuous network inside the particulates, which can thus be expected to be very hard and stiff. An upper bound for the strengthening effect of these particulates is then given by doubling the nominal Mo volume fraction. We use results of Dong and Schmauder,^[15] who modeled the flow behavior of MMCs by a self-consistent embedded cell method for different volume fractions of *entirely rigid* spherical reinforcements embedded in a matrix that obeys a Ramberg-Osgood power law ($\sigma = C(\epsilon/\epsilon_0)^N$). As shown in Figure 15, the flow behavior of the unreinforced reference material of the present study can be represented with good accuracy by such a constitutive law, with $C = 54 \text{ MPa}$, $\epsilon_0 = 1.0 \cdot 10^{-3}$, and $N = 0.17$ (dotted line). The flow curves predicted by the Dong and Schmauder model for 15 or 30 vol pct of rigid particles are shown as dashed lines. It is apparent that, even if we assume the heterogeneous particulates in the Cu/Mo composites to be entirely rigid and to have twice the volume fraction of the Mo phase, the resulting strengthening effect

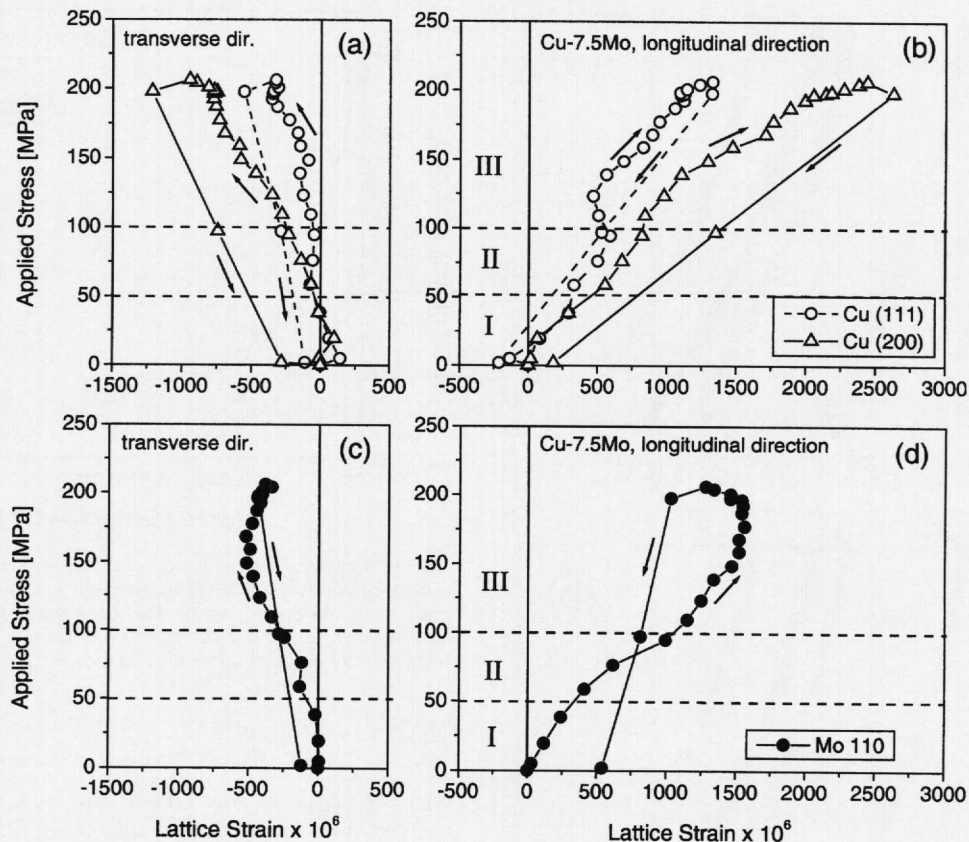


Fig. 11—Applied stress vs lattice strain for the Cu-7.5Mo composite. (a) Cu (111) and Cu (200), transverse direction; (b) Cu (111) and Cu (200), longitudinal direction; (c) Mo (110), transverse direction; and (d) Mo (110), longitudinal direction.

predicted by FE models is still not sufficient to fully explain the observed macroscopic flow curves of the composites (solid lines). We thus conclude that the copper phase in the composites must be significantly stronger than the unreinforced reference material.

Three mechanisms can be proposed to explain this *in-situ* matrix strengthening: (1) grain-boundary hardening, as the presence of the reinforcement particulates causes grain refinement (Table I); (2) strain hardening by mismatch dislocations produced on cooling and depressurization from the HIP temperature and pressure; and (3) dispersion strengthening from molybdenum precipitates, which may form in the copper matrix upon cooling from the HIP temperature. Mechanism (1) is probably not very pronounced, as the grain sizes of composite matrices and that of the unreinforced reference material differ only by a factor of 3 to 4. The corresponding increase in yield stress according to the Hall-Petch equation is 15 to 21 MPa.^[16] Mechanism (2) appears plausible, as fully strain hardened, pure copper exhibits a flow strength of 350 MPa, as compared to a yield stress of 25 MPa.^[17] Geometrically necessary dislocations are expected to be produced upon cooling from the HIP temperature due to the difference of thermal expansion coefficient between Cu and Mo, and, to a lesser extent, upon depressurization from the HIP pressure due to the mismatch in bulk modulus between the two phases. Based on the simplified thermal mismatch calculation given in Reference 18, and depending on the size of the dislocation loops punched by the Mo precipitates, an increase in Cu yield stress of up to 40 MPa can result from mechanism (2). Finally, mechanism

(3) is unlikely to contribute significantly, as the maximum solid solubility of Mo in Cu is 600 ppm at 1083 °C, corresponding to a very small volume fraction of Mo precipitates.

B. Lattice Strains and Load Partitioning Between Phases

Three regimes of load sharing can be identified in the curves of applied stress vs X-ray lattice strain (Figures 10 and 11). At low applied stresses (regime I), load sharing is constant and both phases are expected to behave linear-elastically. At intermediate stresses (regime II), the rate of increase of lattice strain with increasing applied stress decreases in the matrix but increases in the reinforcements. Thus, the fraction of load borne by the matrix decreases, while the reinforcement carries proportionally more load. This type of behavior has been observed in many composites when plastic deformation occurs in the matrix, thus increasing the mismatch with, and load transfer to, the elastic reinforcement.^[1] At even higher applied stresses (regime III), *i.e.*, above about 100 MPa for the Cu-7.5Mo composite and above about 170 MPa for the Cu-15Mo composite, this trend is reversed, indicating that reinforcement is getting less efficiently loaded due to damage accumulation.

In order to assess the load sharing between matrix and reinforcement, average phase stresses rather than average lattice strains are required. However, for the copper matrix, the calculation of average stresses from the measured lattice strains is complicated by elastic anisotropy (which is very pronounced for copper) and by plastic anisotropy (which becomes effective as the matrix yields). To calculate the

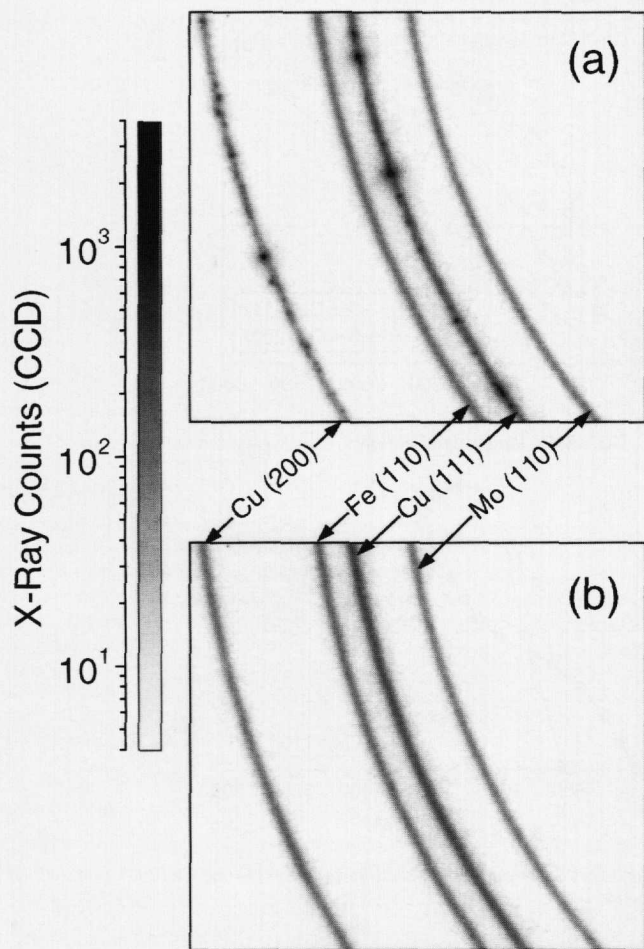


Fig. 12—Closeups of two diffraction patterns (enlargements of the area delineated in Figure 2) recorded during an *in-situ* tensile experiment on a Cu-15Mo sample, showing segments of the Cu (111), Cu (200), and Mo(110) rings from the specimen and the Fe (110) ring from the iron standard powder. It can be seen that the Cu rings are (a) rather grainy initially and (b) become less grainy as the specimen is loaded and deformed, while no significant morphology changes are observed on the Mo(110) and Fe (110) rings.

desired phase stresses under these circumstances, a complex grain interaction model (*e.g.*, References 19 and 20) would have to be adopted to describe the distribution of stresses and strains over grains with different crystallographic orientation, which is beyond the scope of the present study. Moreover, the measured shifts of the copper diffraction peaks may not exclusively be due to stress-induced lattice strains, but partly be caused by changes in stacking fault density occurring during plastic deformation.¹²¹¹ We therefore base our stress analysis on the strains measured for the molybdenum phase, as molybdenum crystals are considerably more isotropic than copper (elastic constants listed in Table II).

We estimate the average reinforcement stress from the Mo(110) lattice strains measured in the longitudinal direction by assuming that the longitudinal stress is independent of the grain orientation and by neglecting the effects of transverse stresses stemming from grain interaction within the reinforcement phase or from interactions between the two phases of the composite. With these simplifying assumptions, the average stress in the molybdenum phase, σ_{Mo} , is estimated as

$$\sigma_{Mo} \approx E_{\langle 110 \rangle, Mo} \cdot \varepsilon_{\langle 110 \rangle, Mo} \quad [11]$$

where $E_{\langle 110 \rangle, Mo} = 319$ GPa is the Young's modulus of a molybdenum single crystal uniaxially loaded in the $\langle 110 \rangle$ direction (Table II) and $\varepsilon_{\langle 110 \rangle, Mo}$ is the lattice strain measured in that direction (Figures 10(d) and 11(d)). The load fraction l_{Mo} carried by the reinforcement is

$$l_{Mo} = f_{Mo} \frac{\sigma_{Mo}}{\sigma_{appl}} \quad [12]$$

where f_{Mo} is the volume fraction of the Mo phase and σ_{appl} is the applied stress. The evolution of this quantity is plotted against the applied strain for both composites in Figure 16. As discussed in Section C, the stresses σ_{Mo} may be overestimated by up to around 60 MPa due to a lattice strain measurement offset caused by unintentional rotation of the specimen during loading. In Figure 16, the corresponding uncertainties of load fractions l_{Mo} are indicated by single-sided error bars. In spite of the large relative errors at small applied strains, it can be seen clearly that the load fraction goes through a maximum for both composites. The decrease in load fractions beyond that maximum (regime III) could be attributed to relaxation of the matrix, plastic deformation of the particulates, or damage processes such as particulate fracture and particulate/matrix detachment. As discussed subsequently, we believe that the dominant process is the disintegration of the particulates consisting of fine, sintered Mo particles infiltrated by copper. The absolute stresses σ_{Mo} that exist in the molybdenum phase around the l_{Mo} maxima in Figure 16 are considerably smaller than the room-temperature yield strength of bulk molybdenum (about 600 MPa²²²). The lattice strain measurements were, however, averaged over a volume that is very large compared to that of a molybdenum particulate. Within the molybdenum phase, stresses and strains vary and may locally be considerably larger than the average value. For instance, stress concentrations at necks connecting the small molybdenum particles agglomerated into a single particulate are likely to lead to

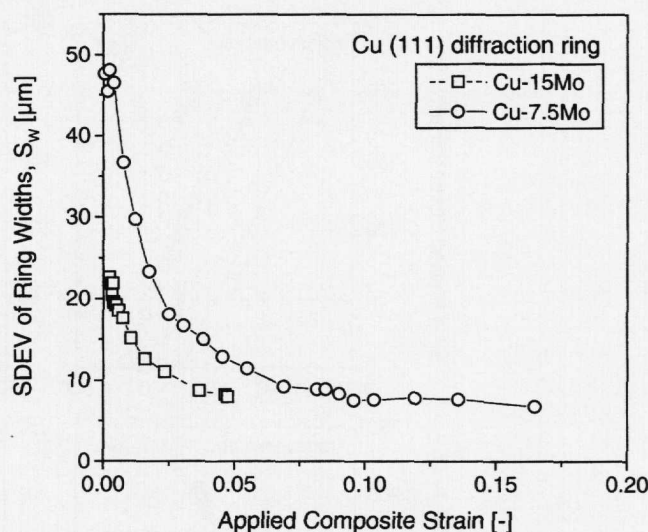
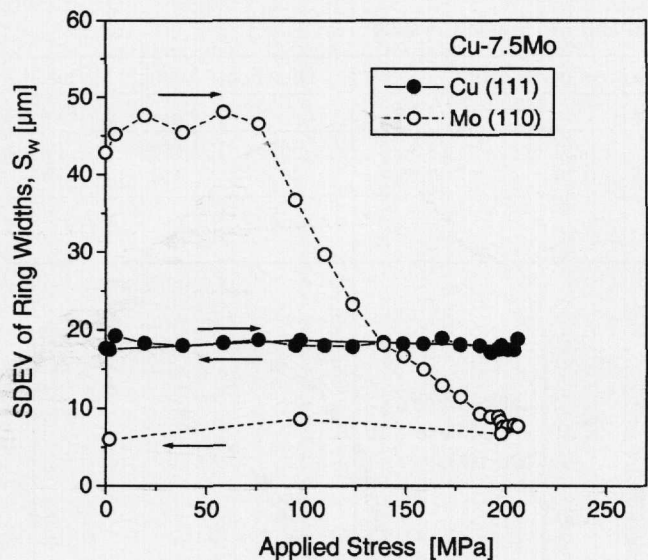
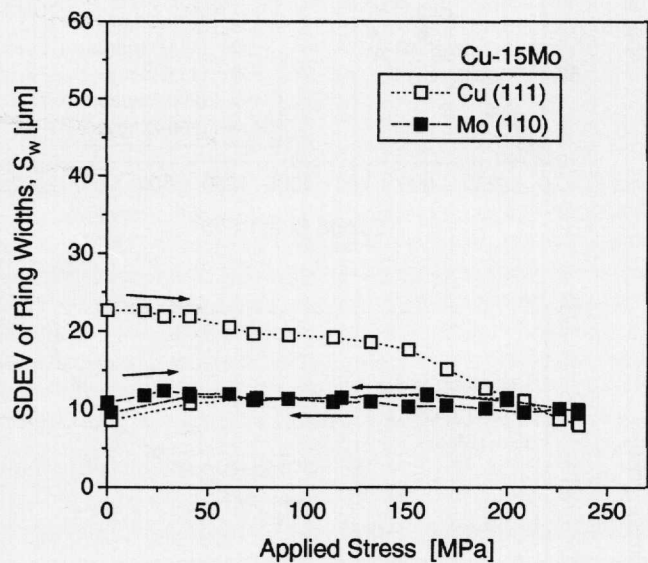


Fig. 13—Dependence of graininess of the Cu (111) diffraction ring on the uniaxial tensile strain applied to the composite specimens (for corresponding stress-strain curves, see Fig. 6). The graininess is assessed by means of the parameter S_w , the standard deviation of the ring widths averaged over 1600 different positions along the ring.



(a)



(b)

Fig. 14—Dependence of the graininess of the Cu (111) and Mo (110) diffraction rings on the uniaxial stress applied to the specimen. The loading-unloading sequence is marked by arrows. (a) Cu-7.5Mo and (b) Cu-15Mo.

disintegration of the particulates as a result of local plastic deformation and fracture at these necks.

The graininess results imply, however, that large-scale plastic deformation did not occur in the molybdenum phase. The graininess of the diffraction rings results from the incident X-ray beam irradiating only a limited number of grains of which only a small fraction are oriented in a diffracting condition. This fraction depends on the broadness of the reciprocal lattice points, which is governed by their real-space size and lattice defect structure. The broader these reciprocal lattice points are, the higher is the fraction of grains that contribute to the diffraction ring and thus the more diffuse are the speckles produced by the individual grains. Hence, for a given number and orientation distribution of grains in the gage volume, the diffraction rings become less grainy if the lattice defect density is increased.

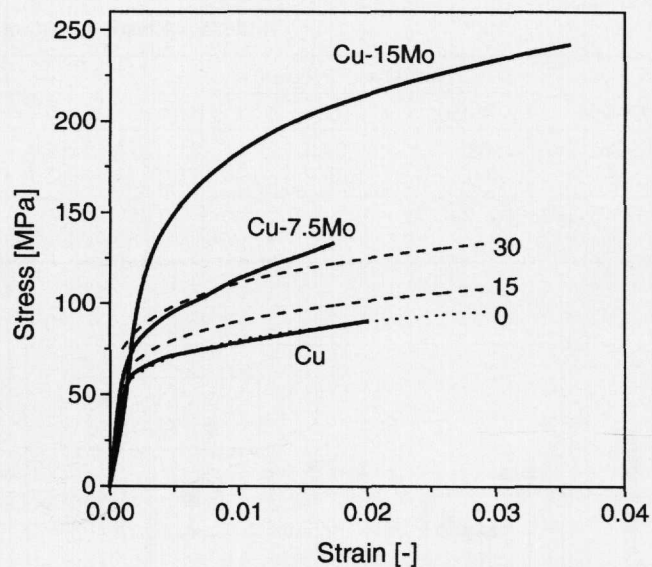


Fig. 15—Comparison of the experimentally determined tensile stress-strain curves of the composites (*ex-situ* curves presented in Fig. 6) to the flow curves predicted by the model by Dong and Schmauder^[15] for rigid particles with 15 or 30 pct volume fraction (dashed lines), assuming that the matrices exhibit the same flow behavior as the unreinforced reference material (dotted line).

Changes in graininess observed upon mechanical loading of the specimen can then be attributed to changes in the defect density of the phase that produces the diffraction ring. Figures 13 and 14 show that defect density increased considerably in the matrix phase, as expected since the matrix must plastically deform to accommodate plastic deformation of the composite. However, no significant changes are observed for the molybdenum phase, indicating that no large-scale plastic deformation occurred in the reinforcement.

C. Methodological Aspects

The present study shows that synchrotron X-ray diffraction experiments can provide valuable information on bulk lattice strains and load partitioning in Cu-Mo composites, despite the fact that both phases have relatively high atomic numbers and X-ray absorption. In the bulk, such metals have so far only been studied by neutron diffraction. In the following, we compare our results to those of Daymond *et al.*,^[7,12,13] who have recently studied the same Cu-15Mo composite by neutron diffraction using a pulsed, polychromatic beam of neutrons produced by a spallation source (for a more detailed description of that technique, we refer to Lewis *et al.*^[4]). As compared to these neutron diffraction measurements, the X-ray exposure times were more than one order of magnitude shorter, although the diffracting volume was about three orders of magnitude smaller in the present study, and this exposure time could be further reduced by the X-ray experiments were performed at an insertion device beamline providing an even brighter beam of photons with even shorter wavelength.

The penetration depth is larger by about one order of magnitude for neutron diffraction, allowing the investigation of considerably thicker specimens. Also, unlike the synchrotron technique, where the diffracted beam must be quite narrow in order to yield narrow diffraction rings, the neutron

Table II. Elastic Constants of Cu and Mo Single Crystals

| Crystal | Stiffness Coefficients* | | | Compliance Coefficients* | | | Directional Young's Moduli** | | |
|---------|-------------------------|----------------|----------------|-------------------------------|-------------------------------|-------------------------------|------------------------------|---------------|---------------|
| | C_{11} (GPa) | C_{12} (GPa) | C_{44} (GPa) | S_{11} (TPa ⁻¹) | S_{12} (TPa ⁻¹) | S_{44} (TPa ⁻¹) | $E_{(100)}$ * | $E_{(110)}$ * | $E_{(111)}$ * |
| Cu | 168 | 121 | 75 | 15.0 | -6.28 | 13.3 | 67 | 130 | 190 |
| Mo | 460 | 176 | 117 | 2.76 | -0.76 | 8.55 | 363 | 319 | 307 |

*According to Ref. 25.

$$**1/E_{(hkl)} = S_{11} - (2S_{11} - 2S_{12} - S_{44})(h^2k^2 + k^2l^2 + l^2h^2)/(h^2 + k^2 + l^2)^2.[26]$$

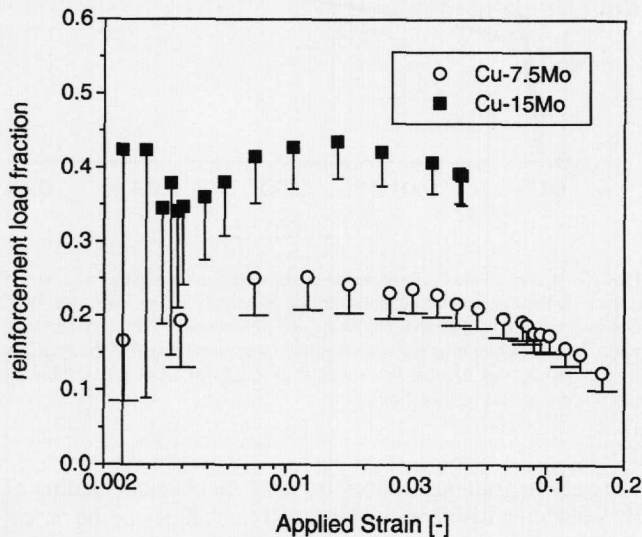


Fig. 16—Dependence of the reinforcement load fraction $f_{Mo} = f_{Mo} \cdot \sigma_{Mo} / \sigma_{app}$ on applied strain.

technique uses a much wider incident beam, leading to a considerably larger gage volume, typically by three or more orders of magnitude. However, the large diffraction volume is also a prerequisite for neutron diffraction because of the weak interaction of thermal neutrons with most nuclei, leading to prohibitively long measurement times for very small volumes. While the small diffraction volume of the synchrotron X-ray transmission technique has a number of positive aspects (small quantities of specimen material are required to fabricate tensile specimens, high-resolution strain mapping is possible, etc.), it also limits its application to fine-grained specimen materials. The ellipse fitting procedure proposed in the present work has proved to be an excellent tool to raise the level of tolerable diffraction ring graininess significantly.

In Figure 17, the longitudinal lattice strains measured on the Cu-15Mo composite are compared with the neutron diffraction results obtained by Daymond *et al.* during their *in-situ* tensile tests on the same material. These authors applied stresses up to about 160 MPa, thus limiting their investigation to regimes I and II of load partitioning. While carrying out fits on single diffraction peaks allows determination of elastic strain for the corresponding crystallographic direction, it is usual at a pulsed neutron source to average over a large number of peaks using a Rietveld refinement procedure,^[19, 23] which has been shown to provide a good measure of the bulk average elastic strain.^[24] In Figures 17(a) and (b), the Rietveld refinement results^[7] as well as previously unpublished “single-peak” lattice strains from

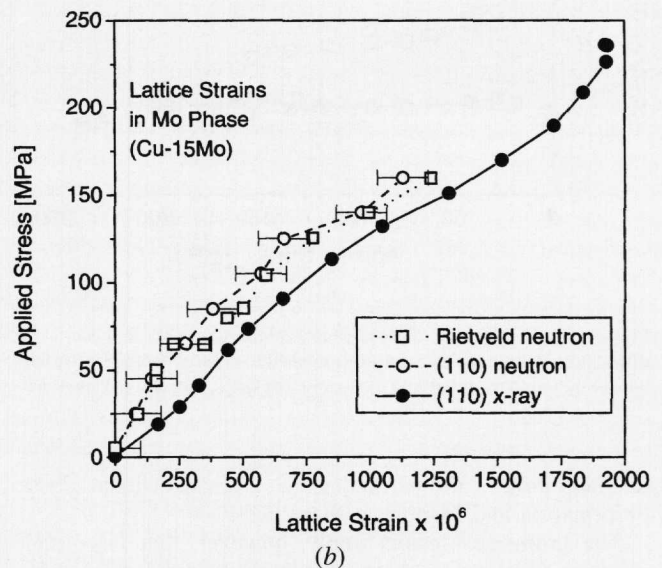
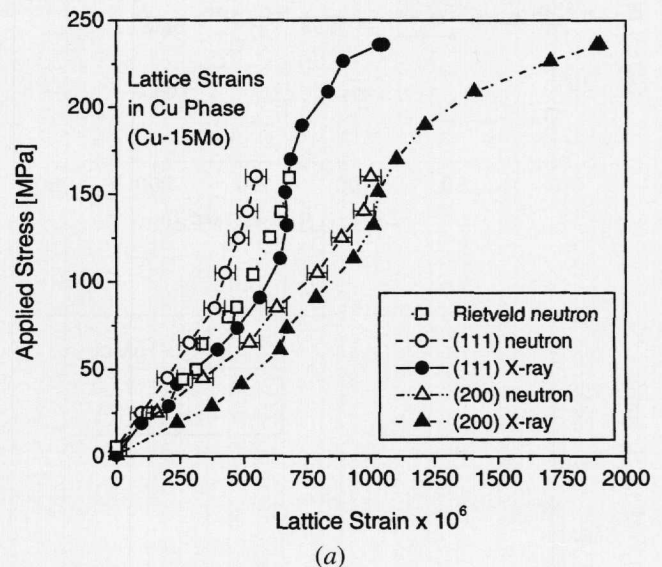


Fig. 17—Applied stress vs lattice strain in longitudinal direction for Cu-15Mo. Comparison of the results of the present study with Daymond *et al.*'s results from evaluation of individual peaks^[12] and from Rietveld analysis of multiple peaks^[7] (neutron diffraction experiments): (a) copper phase and (b) molybdenum phase.

analyzing the shifts of the Mo (110), Cu (111), and Cu (200) neutron diffraction peaks^[12] are shown, along with the corresponding single-peak lattice strains of the present study. The agreement between corresponding X-ray and neutron curves is satisfactory in the sense that the general trends and curve shapes are the same. However, for all three sets of

single-peak results above 50 MPa, X-ray diffraction lattice strains were systematically larger than neutron diffraction results by about 200 μ strains. This suggests that the X-ray results exhibit a systematic error, which is gradually introduced in an early stage of the *in-situ* experiment, *i.e.*, at low applied stresses, where the largest specimen displacements occurred (Figure 8). To determine why our correction procedure (Eq. [10]) did not eliminate the effects of specimen movement entirely, we performed an additional *ex-situ* tensile test to examine in more detail the nature of the specimen movements occurring during loading and unloading. We found that the specimen is not only translated by several tenths of a millimeter, but also rotated around its longitudinal axis by up to about 15 deg during the first two steps of loading. These rotations are caused by the single-screw design of the screw-driven miniature tensile device. Our correction procedure, however, was based on the assumption that the spacing between specimen and calibration substance remained unchanged, which is true as long as the specimen is only translated in space, but not when it is rotated around any axis that does not coincide with the direction of the X-ray beam. Rotation around the loading axis by a small angle α causes the *effective* specimen-to-calibration substance spacing ΔL to increase by a factor of $1/\cos\alpha$. Starting from $\Delta L = 2.52$ mm, the increase is 89 μ m for $\alpha = 15$ deg. This corresponds to a lattice strain error of $89 \mu\text{m}/510 \text{ mm} = 175 \mu\text{strain}$, which is close to the 200 μ strain offset observed in Figure 17. By limiting specimen rotations to less than about 3 deg, which can in our case be accomplished *via* minor changes in the design of the loading rig, the error can be reduced to less than 7 μ strain, which is negligible.

In summary, unintentional specimen movements bear a huge potential as a source of measurement error and must therefore be eliminated or tightly controlled. The present study shows that, by using a calibration substance attached to the specimen under investigation, errors from specimen translation can be eliminated. Specimen rotations must be limited to a few degrees, because their effect is not compensated by the correction procedure based on the calibration substance. By following these guidelines, the accuracy of lattice strain measurements with the synchrotron X-ray transmission technique is similar to that of careful neutron diffraction measurements, making the synchrotron technique a powerful internal strain measurement tool, which is complementary to the well-established neutron diffraction technique.

VI. SUMMARY

The present work has shown that synchrotron X-ray diffraction experiments can provide valuable and fast bulk lattice strain measurements and load partitioning information in a metallic material consisting of chemical elements with relatively high atomic numbers and thus X-ray absorption.

Lattice strain measurements with the high-energy X-ray transmission technique are made difficult by two effects: (1) the graininess of the diffraction rings caused by the relatively small diffracting volume and (2) strong sensitivity to unintentional movement of the specimen under investigation. These issues were investigated in detail and strategies to eliminate or minimize the related measurement errors were developed. It was shown that the effects of specimen movement can largely be eliminated by means of a calibration

substance attached to the specimen and that the effects of diffraction ring graininess can be minimized by applying a sophisticated data fitting procedure.

The improved measurement technique was applied to study the evolution of elastic phase strains in copper matrix composites reinforced with agglomerated molybdenum particles during *in-situ* uniaxial tensile deformation. The lattice strains in the molybdenum phase were used to estimate the load fraction carried by the reinforcements, which was found to vary significantly in the course of the deformation of the composite. At small applied strains, load transfer from the yielding matrix to the elastic reinforcements was observed. At larger strains (*i.e.*, at about 1 to 2 pct total deformation), the load fraction carried by the reinforcements reached a maximum and then decreased continuously. This reversal of load transfer was attributed to the disintegration of the reinforcement particulates, which consisted of fine, sintered molybdenum particles infiltrated by copper.

ACKNOWLEDGMENTS

This paper is dedicated to the memory of Professor Jerome B. Cohen (Northwestern University) who introduced us to the technique of synchrotron X-ray diffraction, lent us his miniature tensile device, and encouraged us through many helpful discussions. We also thank Dr. Mark R. Daymond (ISIS, Harwell, United Kingdom) for providing unpublished neutron single-peak data presented in Figures 17(a) and (b). AW gratefully acknowledges the Max Kade Foundation (New York, NY) as well as the Eshbach Society (Evanston, IL) for supporting his stay at Northwestern University, during which the experimental work was performed. The diffraction experiments were performed at the DuPont-Northwestern-Dow Collaborative Access Team (DND-CAT) Synchrotron Research Center located at the Advanced Photon Source (Argonne National Laboratory, IL), whose staff we acknowledge for their excellent technical support. DND-CAT is supported by the E.I. DuPont de Nemours & Co., The Dow Chemical Company, the United States National Science Foundation through Grant No. DMR-9304725, and the State of Illinois through Grant No. IBHE HECA NWU 96. Use of the Advanced Photon Source was supported by the United States Department of Energy under Contract No. W-31-102-Eng-38.

REFERENCES

1. T.W. Clyne and P.J. Withers: *An Introduction to Metal Matrix Composites*, Cambridge University Press, Cambridge, United Kingdom, 1993.
2. A.J. Allen, M.A.M. Bourke, S. Dawes, M.T. Hutchings, and P.J. Withers: *Acta Metall. Mater.*, 1992, vol. 40, pp. 2361-73.
3. M.A.M. Bourke, J.A. Goldstone, M.G. Stout, A.C. Lawson, and J.E. Allison: *Scripta Metall. Mater.*, 1993, vol. 29, pp. 771-76.
4. C.A. Lewis, W.M. Stobbs, and P.J. Withers: *Mater. Sci. Eng. A*, 1993, vol. A171, pp. 1-11.
5. D.C. Dunand, D. Mari, M.A.M. Bourke, and J.A. Roberts: *Metall. Mater. Trans. A*, 1996, vol. 27A, pp. 2820-36.
6. R. Vaidyanathan, M.A.M. Bourke, and D.C. Dunand: *Acta Mater.*, 1999, vol. 47, pp. 3353-66.
7. M.R. Daymond, C. Lund, M.A.M. Bourke, and D.C. Dunand: *Metall. Mater. Trans. A*, 1999, vol. 30A, pp. 2989-97.
8. I.C. Noyan and J.B. Cohen: *Residual Stress—Measurement by Diffraction and Interpretation*, Springer-Verlag, New York, NY, 1987.
9. M.R. Daymond and P.J. Withers: *Scripta Mater.*, 1996, vol. 35, pp. 1229-34.

10. A.M. Korsunsky, K.E. Wells, and P.J. Withers: *Scripta Mater.*, 1998, vol. 39, pp. 1705-12.
11. A. Wanner and D.C. Dunand: *Mater. Res. Soc. Symp. Proc.*, 2000, vol. 590, pp. 157-162.
12. M.R. Daymond: ISIS Department, Rutherford-Appleton Lab., Harwell, United Kingdom, personal communication.
13. C. Lund: Master's Thesis, Massachusetts Institute of Technology, Cambridge, MA, 1997.
14. P.R. Subramanian and D.E. Laughlin: in *Binary Alloy Phase Diagrams*, 2nd ed., T.B. Massalski, ed., ASM INTERNATIONAL, Materials Park, OH, 1990, vol. 2.
15. M. Dong and S. Schmauder: *Acta Mater.*, 1996, vol. 44, pp. 2465-78.
16. M.A. Meyers and K.K. Chawla: *Mechanical Behavior of Materials*, Prentice-Hall, Englewood Cliffs, NJ, 1999, p. 272.
17. E. El Danaf, S.R. Kalindi, and R.D. Doherty: *Metall. Mater. Trans. A*, 1999, vol. 30A, pp. 1223-33.
18. D.C. Dunand and A. Mortensen: *Acta Metall. Mater.*, 1991, vol. 39, pp. 127-39.
19. M.R. Daymond, M.A.M. Bourke, R.B. Von Deele, B. Clausen, and T. Lorentzen: *J. Appl. Phys.*, 1997, vol. 82, pp. 1554-62.
20. M. van Leeuwen, J.-D. Kamminga, and E.J. Mittemeijer: *J. Appl. Phys.*, 1999, vol. 86, pp. 1904-14.
21. L.H. Schwartz and J.B. Cohen: *Diffraction from Materials*, Academic Press, New York, NY, 1977, ch. 7.5.
22. H.E. Boyer: *Atlas of Stress-Strain Curves*, ASM International, Metals Park, OH, 1987.
23. H.M. Rietveld: *J. Appl. Cryst.*, 1969, vol. 2, pp. 65-71.
24. M.R. Daymond, M.A.M. Bourke, and R.B. von Dreele: *J. Appl. Phys.*, 1999, vol. 85, pp. 739-47.
25. T.H. Courtney: *Mechanical Behavior of Materials*, McGraw-Hill, New York, NY, 1990, p. 59.
26. J.F. Nye: *Physical Properties of Crystals*, Oxford University Press, Oxford, United Kingdom, 1985, pp. 143-45.